Spatio-angular fluorescence microscopy I. Basic theory

TALON CHANDLER,[1,*] AUTHOR ORDER TBD,[2,*] AND PATRICK LA RIVIÈRE [1]

[1]*University of Chicago, Department of Radiology, Chicago, Illinois 60637, USA*
[2]*Publications Department, The Optical Society, 2010 Massachusetts Avenue NW, Washington, DC 20036, USA*
[3]*Currently with the Department of Electronic Journals, The Optical Society, 2010 Massachusetts Avenue NW, Washington, DC 20036, USA*
talonchandler@talonchandler.com

Abstract: We introduce the basic elements of a spatio-angular theory of fluorescence microscopy. We start by analyzing a paraxial single-view fluorescence microscope imaging an ensemble of in-focus fluorophores without using the monopole or scalar approximations. We define and calculate the spatio-angular transfer function (SATF) and show that fluorescence microscopes have an angular band limit. We demonstrate the value of the transfer function approach by efficiently simulating the imaging process with numerical phantoms. Notably, we show that information about the out-of-plane orientation of in-focus fluorophores is imaged in paraxial widefield fluorescence microscopes. We discuss the implications of our analysis for all quantitative fluorescence microscopy studies.

1. Introduction

Fluorescence microscopes are widely used in biology [XXX], materials science [XXX], and metrology [XXX] for measuring the distribution of fluorophores throughout a sample. While an unprocessed fluorescence micrograph reports the approximate distribution of fluorophores throughout a sample, all microscopes are diffraction limited, so the image is a blurred version of the true fluorophore distribution. Therefore, microscopists who are interested in optimal measurements will perform a computational restoration to recover some of the information lost during the imaging process.

Restoration techniques attempt to recover the true distribution of fluorophores using the measured data and a model of the imaging process. A model of the imaging process can be obtained theoretically (by mathematically modeling the instrument under idealized conditions), experimentally (by measuring the instrument's response to a known input), or by a combination of theory and experiment (by measuring parameters of an instrument model). In all cases the accuracy of the restored fluorophore distribution is limited by the accuracy of the imaging model.

All theoretical imaging models of make simplifying approximations that limit the accuracy of restorations, so it is important to verify that the approximations introduce an acceptable level of error. This work investigates the errors introduced by two common approximations in models of fluorescence microscopes—the *monopole approximation* and the *scalar approximation*.

by ignoring the dipole excitation and emission processes and to (2) treat light propagation under the *scalar approximation* by ignoring the polarization of light. These approximations can limit the accuracy of restoration in all types of fluorescence microscopes. The goal of this work is to analyze fluorescence microscopes without these approximations and find the conditions under which these approximations are justified.

This work lies at the intersection of three classes of fluorescence microscopy: (1) single-molecule localization microscopy (SMLM), (2) spatial ensemble fluorescence microscopy including widefield, confocal, and light-sheet techniques, and (3) polarized fluorescence microscopy. We briefly review these three classes and focus on their use of the monopole and scalar

approximations.

The SMLM community has pioneered the use of rigorous electromagnetic models of fluorescence microscopes [1, 2] [Novotny]. When a single molecule is fluorescing in the sample, the measured intensity pattern is strongly dependent on the orientation of the emitting molecule. Backlund and Lew [3] have shown that ignoring the orientation of fluorophores can bias position estimates. Therefore, the most accurate SMLM experiments must jointly estimate the position and orientation of each molecule.

A major limitation of SMLM experiments is speed

Meanwhile, most fluorescence microscopists image ensembles of fluorophores and restore their images without considering the role that the monopole and scalar approximations play in the restoration process. A typical fluorescence microscopist is only interested in the spatial distribution of fluorophores, so they reason (possibly erroneously) that they can ignore the orientation of the emitters.

A smaller community of microscopists is interested in measuring the orientation of ensembles of fluorophores [4] [Forkey, Goldman, Moerner]. These techniques typically use a combination of Current restoration techniques use a model of the dipole excitation and emission process to restore the orientation of fluorophores using pixel-wise arithmetic, but these techniques do not perform any spatial restoration so they are sub-optimal. To our knowledge no work has been done to model the complete spatio-angular response of fluorescence microscopes to ensembles of oriented fluorophores.

In this work we model ensembles of in-focus dipole absorber/emitters using electromagnetic optics and the paraxial approximation. In section 2 we model the excitation and detection processes of dipoles, and we define the most important quantity in this work—the spatio-angular transfer function (SATF). We calculate the SATF and show that fluorescence microscopes have an angular band limit. In section 3 we perform simulations and compare our model to traditional scalar models. In section 4 we discuss the implications of our work for fluorescence microscopy and lay out a path towards a complete spatio-angular theory of fluorescence microscopy.

2. Theory

Consider a single dipole radiator at the origin with its dipole moment oriented along a direction $\hat{\mathbf{s}}_o$. The dipole emitter creates a time-harmonic electric field at a position $\mathbf{r}$ far from the dipole proportional to

$$\mathbf{E}_{\text{ff}}(\mathbf{r}, \hat{\mathbf{s}}_o) \propto \frac{\exp[ik|\mathbf{r}|]}{|\mathbf{r}|} \hat{\mathbf{r}} \times \hat{\mathbf{s}}_o \times \hat{\mathbf{r}}. \tag{1}$$

A typical approach to deriving Equation 1 is to (1) use Maxwell's equations to derive the inhomogeneous electromagnetic wave equations then (2) use potentials to solve the wave equations with a dipole source term, then (3) drop the terms that decay faster than $1/|\mathbf{r}|$—see Jackson, Novotny, Teich for clear expositions. Equation 1 succinctly shows that dipole radiators emit spherical wavefronts of polarized light with amplitude proportional to $\cos\theta$ where θ is the angle between the field point $\mathbf{r}$ and the dipole axis $\hat{\mathbf{s}}_o$.

Many models of fluorophores approximate the vector field on the left hand side of Equation 1 with a scalar field—the *scalar approximation*—and drop the orientation dependence on the right hand side—the *monopole approximation*. The approximated field is given by

$$U_{\text{ff}}(\mathbf{r}) \propto \frac{\exp[ik|\mathbf{r}|]}{|\mathbf{r}|}. \tag{2}$$

Models that use Equation 2 as a starting point do not account for polarization or dipole orientation effects. In Section 2.1 we will review the derivation of the monopole imaging model starting with Equation 2. These results are widely known, but they serve as a review of the concepts we

will need for the dipole imaging case. In Section 2.2 will derive a dipole imaging model starting with Equation 1. Finally, in Section 2.3 we will calculate the SATF for the dipole imaging model.

2.1. Monopole imaging model

We briefly analyze a paraxial $4f$ fluorescence imaging system using the monopole and scalar approximations—a similar treatment can be found in [5]. We start by considering a field of in-focus monopoles that have been excited by a spatially uniform beam. As the fluorophores relax, they emit scalar waves in the form of Equation 2. The waves propagate through the microscope and we measure the irradiance on a two dimensional detector.

We can represent the object as a two-dimensional function $f(\mathbf{r}_o)$ that we call the *monopole density*—the number of monopoles at position $\mathbf{r}_o$ per unit area. In the language of image science, we say that $f(\mathbf{r}_o)$ is a member of the set of square integrable functions on the plane $\mathbb{L}_2(\mathbb{R}^2)$. The data we collect is the irradiance on a plane $g(\mathbf{r}_d)$, so the data is a member of the same set $\mathbb{L}_2(\mathbb{R}^2)$.

A reasonable starting point is to assume that the relationship between the object and the data is *linear*—this seems plausibly since a scaled sum of monopoles will result in a scaled sum of the irradiance patterns created by the individual monopoles. Therefore, we can write the irradiance as the integral over a field of monopoles weighted by the detector response due to single monopoles

$$g(\mathbf{r}_d) = \int_{\mathbb{R}^2} d\mathbf{r}_o \, h(\mathbf{r}_d, \mathbf{r}_o) f(\mathbf{r}_o). \tag{3}$$
Monopole imaging model

where $h(\mathbf{r}_d, \mathbf{r}_o)$ is the kernel of the integral transform.

The first step is to calculate the field in the back focal plane of the objective lens. We can model a paraxial thin lens as a quadratic phase element, so it converts a spherical wave to a plane wave in the back focal plane with a sharp cutoff at the exit pupil of the lens

$$U_{\text{bfp}}(\mathbf{r}_b) \propto \Pi\left(\frac{|\mathbf{r}_b|}{\alpha}\right) \equiv \begin{cases} 1 & \text{if} \quad |\mathbf{r}_b| < \alpha, \\ 0 & \text{else.} \end{cases} \tag{4}$$

A central result of Fourier optics is that the fields one focal distance from either side of a paraxial lens are related by a scaled two-dimensional Fourier transform. If we place a detector in the focal plane of the tube lens then the field on the detector is given by

$$U_{\text{det}}(\mathbf{r}_d) \propto \mathcal{F}_{\mathbb{R}^2}\left\{U_{\text{bfp}}(\mathbf{r}_b)\right\} = \frac{J_1(k\alpha|\mathbf{r}_d|)}{k\alpha|\mathbf{r}_d|}. \tag{5}$$

Finally, the detector measures the irradiance instead of the field, so we take the modulus squared of the field to find that the measurable image of a single monopole radiator at the origin is the familiar Airy disk

$$h(\mathbf{r}_d, \mathbf{r}_o = 0) \propto |U_{\text{det}}(\mathbf{r}_d)|^2 = \left[\frac{J_1(k\alpha|\mathbf{r}_d|)}{k\alpha|\mathbf{r}_d|}\right]^2. \tag{6}$$

Shifting the monopole in the transverse plane will introduce a linear phase factor in the back focal plane which will manifest as a shift on the detector. Therefore, our imaging system is shift invariant and we can rewrite the irradiance on the detector due to a monopole at $\mathbf{r}_o$ as

$$h(\mathbf{r}_d, \mathbf{r}_o) = h(\mathbf{r}_d - \mathbf{r}_o). \tag{7}$$

For convenience we have used the same letter for both functions in Equation 7 even though they have a different number of variables. We will continue to rewrite functions with fewer variables

in the same way throughout this paper. Also, Equation 7 only applies directly to microscopes with unit magnification, but a similar relationship can be found for magnifying microscopes by making a change of variables—see Barrett section 7.2.7.

Rotating a monopole will leave its image unchanged. Therefore, our imaging system is rotation invariant and we can simplify the kernel further with

$$h(\mathbf{r}_d - \mathbf{r}_o) = h(|\mathbf{r}_d - \mathbf{r}_o|). \tag{8}$$

In the language of image science, Equation 3 specifies an integral transform relationship between objects that are members of the space of square-integrable functions on the plane $\mathbb{U} = \mathbb{L}_2(\mathbb{R}^2)$ and data that lives in the same space $\mathbb{V} = \mathbb{L}_2(\mathbb{R}^2)$. We can rewrite Equation 3 more abstractly as

$$\mathbf{g} = \mathcal{H}\mathbf{f} \tag{9}$$

where $\mathcal{H} : \mathbb{L}_2(\mathbb{R}^2) \rightarrow \mathbb{L}_2(\mathbb{R}^2)$ is the forward operator of the imaging system. We say that the shift invariance and rotational invariance introduced in Equations 7 and 8 are *symmetries of the forward operator*. Specifying a linear operator that maps $\mathbb{L}_2(\mathbb{R}^2)$ to $\mathbb{L}_2(\mathbb{R}^2)$ always requires us to specify a kernel in the set $\mathbb{L}_2(\mathbb{R}^4)$, but we can exploit the symmetries of the forward operator to specify the complete kernel with a "smaller" function in the set $\mathbb{L}_2(\mathbb{R})$.

Just as a finite-dimensional linear operator can be represented by a matrix in a specific basis, the infinite-dimensional linear operator in Equation 9 can be represented by an integral transform in a specific basis. Equation 3 is an integral transform representation of the monopole imaging process in a *spatial basis* with basis functions of the form $\delta(\mathbf{r} - \mathbf{r}_o)$, but this is not always the best choice. We can exploit the shift-invariance of the forward operator by choosing basis functions of the form $\exp[i2\pi\mathbf{r} \cdot \nu]$ and use the Fourier transform to reexpress the monopole imaging model in a *spatial-frequency basis* as

$$G(\nu) = H(\nu)F(\nu) \tag{10}$$

where ν is a two-dimensional spatial frequency, $G(\nu)$ is the spectrum of the irradiance, $F(\nu)$ is the spectrum of the monopole density, and $H(\nu)$ is the two-dimensional optical transfer function. Because the fast Fourier transform provides an efficient method to change between the spatial and spatial-frequency bases, Equation 10 provides a computational advantage over Equation 3 because we only need to multiply two functions in $\mathbb{L}_2(\mathbb{R}^2)$.

The optical transfer function above exploits shift invariance but does not exploit rotational invariance. We can define a similar transfer function that exploits both shift and rotational invariance by choosing the same Fourier basis (see Barrett 7.2.9 for related discussion) and express the transfer function as a member of the set $\mathbb{L}_2(\mathbb{R})$

$$G(\nu) = H(|\nu|)F(\nu). \tag{11}$$

2.2. Dipole imaging model

We seek to extend the monopole imaging model to dipoles. Comparing Equations 1 and 2 shows that we will need to consider the orientation of the dipole radiators. We also notice that both monopoles and dipoles emit spherical wavefronts, so our argument for shift invariance in the monopole imaging model holds for the dipole imaging model as well. Finally, it is reasonable to assume that rotational invariance will be maintained under the paraxial approximation. Therefore, we can plausibly extend the monopole imaging model in Equation 3 to dipoles with

$$g(\mathbf{r}_d) = \int_{\mathbb{S}^2} d\hat{\mathbf{s}}_o \int_{\mathbb{R}^2} d\mathbf{r}_o \, h(\mathbf{r}_d, \mathbf{r}_o, \hat{\mathbf{s}}_o) f(\mathbf{r}_o, \hat{\mathbf{s}}_o). \tag{12}$$
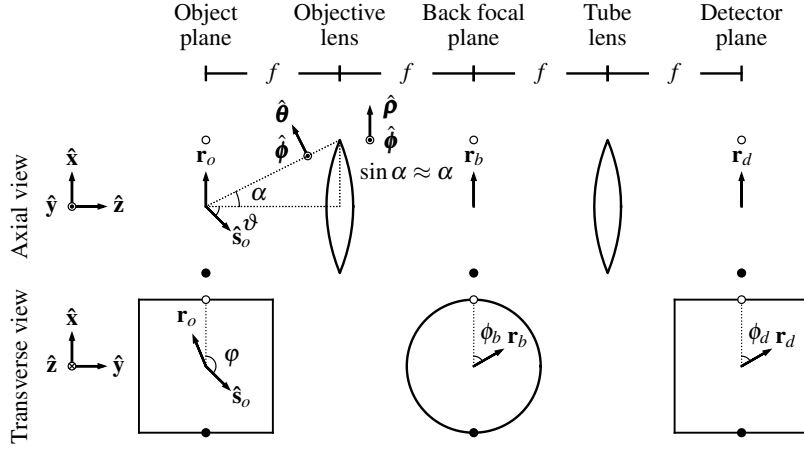
Dipole imaging model
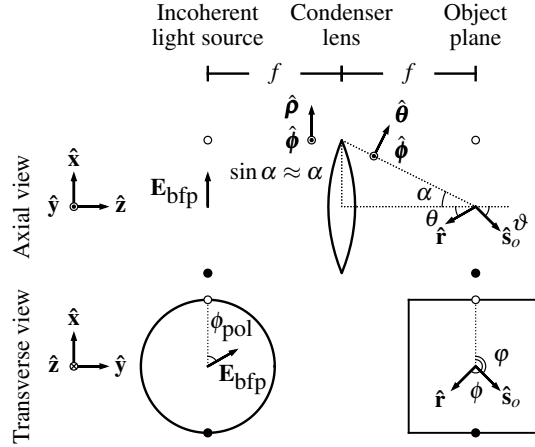
Fig. 1. Detection geometry and coordinates.

Fig. 2. Illumination geometry and coordinates.

where $f(\mathbf{r}_o, \hat{\mathbf{s}}_o)$ is the *spatio-angular density*—the number of dipoles at position $\mathbf{r}_o$ per unit area oriented along $\hat{\mathbf{s}}_o$ per unit solid angle—and $\mathbb{S}^2$ is the unit sphere. Notice that the functional form of our data is left unchanged $\mathbb{V} = \mathbb{L}_2(\mathbb{R}^2)$ while we have extended the set of possible objects to $\mathbb{U} = \mathbb{L}_2(\mathbb{R}^2 \times \mathbb{S}^2)$. Similar to the monopole case, the most general linear operator mapping between these two spaces would require a kernel in $\mathbb{L}_2(\mathbb{R}^4 \times \mathbb{S}^2)$, but we can exploit symmetries and specify the complete kernel with a function in $\mathbb{L}_2(\mathbb{R} \times \mathbb{S}^2)$.

At this point we have only asserted the plausibility of Equation 12—we still need to calculate the form of the kernel $h(r, \hat{\mathbf{s}}_o)$. Our first step is to notice that the kernel can be separated into the product of an excitation part and a detection part

$$h(r, \hat{\mathbf{s}}_o) = h_{\text{exc}}(\hat{\mathbf{s}}_o)\, h_{\text{det}}(r, \hat{\mathbf{s}}_o).$$ (13)

In the next two subsections we will calculate the excitation and detection kernels explicitly.

2.2.1. Dipole excitation model

When we developed the monopole imaging model we ignored the excitation process because we excited the fluorophores with a spatially uniform excitation beam and monopoles have no orientation dependence. For the dipole imaging model we must account for the excitation process because the excitation process is not angularly uniform (except for carefully calibrated TIRF systems).

In this section we will calculate the excitation kernel $h_{\text{exc}}(\hat{\mathbf{s}}_o)$ for epi-illuminationn microscopes. We can interpret $h_{\text{exc}}(\hat{\mathbf{s}}_o)$ as the relative probability of exciting a molecule with dipole orientation $\hat{\mathbf{s}}_o$. Our approach is similar to previous work [6, 7], but here we consider unpolarized and incoherent illumination and restrict ourselves to the paraxial approximation.

We start by expressing the dipole moment $\hat{\mathbf{s}}_o$ in spherical coordinates [see Fig. 1(a)] as

$$\hat{\mathbf{s}}_o = \cos\varphi\sin\vartheta\hat{\mathbf{x}} + \sin\varphi\sin\vartheta\hat{\mathbf{y}} + \cos\vartheta\hat{\mathbf{z}}. \tag{14}$$

We can rewrite Eq. 14 in terms of spherical harmonic functions (see Appendix A) as

$$\hat{\mathbf{s}}_o = \sqrt{\frac{3}{4\pi}}\left[y_1^1(\vartheta,\varphi)\,\hat{\mathbf{x}} + y_1^{-1}(\vartheta,\varphi)\,\hat{\mathbf{y}} + y_1^0(\vartheta,\varphi)\,\hat{\mathbf{z}}\right]. \tag{15}$$

We place the dipole in the focal plane of an aplanatic and polarization-preserving objective lens with its optical axis aligned with the $\hat{\mathbf{z}}$ axis. Next, we place a spatially incoherent, spatially uniform, unpolarized thermal light source (or its image) in the back aperture of the objective lens to illuminate the focal plane. In this geometry each point in the back focal plane generates a plane wave that illuminates the sample.

To model the unpolarized light source we will use polarized ray tracing [cite Torok] to find the response for a single polarized ray, then integrate over the rays and polarizations to find the complete response. First, we model the electric field at every point on the back focal plane as

$$\mathbf{E}_{\text{bfp}}(\phi_{\text{pol}}) \propto \cos\phi_{\text{pol}}\hat{\mathbf{x}} + \sin\phi_{\text{pol}}\hat{\mathbf{y}}, \tag{16}$$

where ϕ_{pol} is the polarization orientation and $\{\hat{\mathbf{x}}, \hat{\mathbf{y}}\}$ are transverse Cartesian basis vectors. Note that Eq. 16 describes the incoherent electric fields at every point in the back focal plane— it does not describe a coherent plane wave. Immediately after the lens the electric field is

$$\mathbf{E}_{\text{ff}}(\theta, \phi, \phi_{\text{pol}}) \propto \left\{[\mathbf{E}_{\text{bfp}}(\phi_{\text{pol}}) \cdot \hat{\boldsymbol{\phi}}]\,\hat{\boldsymbol{\phi}} + [\mathbf{E}_{\text{bfp}}(\phi_{\text{pol}}) \cdot \hat{\boldsymbol{\rho}}]\,\hat{\boldsymbol{\theta}}\right\}\sqrt{\cos\theta}, \tag{17}$$

where $\{\theta, \phi\}$ are spherical coordinates, $\{\hat{\boldsymbol{\rho}}, \hat{\boldsymbol{\phi}}\}$ are cylindrical basis vectors, and $\{\hat{\boldsymbol{\theta}}, \hat{\boldsymbol{\phi}}\}$ are spherical basis vectors defined in Figure 1(a) and related by

$$\hat{\boldsymbol{\rho}} = \cos\phi\hat{\mathbf{x}} + \sin\phi\hat{\mathbf{y}}, \tag{18}$$

$$\hat{\boldsymbol{\phi}} = -\sin\phi\hat{\mathbf{x}} + \cos\phi\hat{\mathbf{y}}, \tag{19}$$

$$\hat{\boldsymbol{\theta}} = \cos\phi\cos\theta\hat{\mathbf{x}} + \sin\phi\cos\theta\hat{\mathbf{y}} - \sin\theta\hat{\mathbf{z}}. \tag{20}$$

In Eq. 17 the $[\mathbf{E}_{\text{bfp}}(\phi_{\text{pol}}) \cdot \hat{\boldsymbol{\phi}}]\,\hat{\boldsymbol{\phi}}$ term models s-polarized fields, the $[\mathbf{E}_{\text{bfp}}(\phi_{\text{pol}}) \cdot \hat{\boldsymbol{\rho}}]\,\hat{\boldsymbol{\theta}}$ term models the rotation of p-polarized fields, and the $\sqrt{\cos\theta}$ term models the apodization of an aplanatic lens. After plugging Eqs. 16, 18, 19, and 20 into Eq. 17 and applying the paraxial approximation, the electric field immediately after the lens is given by

$$\mathbf{E}_{\text{ff}}^{(p)}(\theta, \phi, \phi_{\text{pol}}) \propto \cos\phi_{\text{pol}}\hat{\mathbf{x}} + \sin\phi_{\text{pol}}\hat{\mathbf{y}} - \theta\cos(\phi - \phi_{\text{pol}})\hat{\mathbf{z}}. \tag{21}$$

The probability that a dipole oriented along $\hat{\mathbf{s}}_o$ is excited by a ray with electric field $\mathbf{E}$ is given by $|\mathbf{E} \cdot \hat{\mathbf{s}}_o|^2$. Evaluating this expression for each ray would be cumbersome if we used Eqs. 14 and

21 because we would need to simplify a large number of trigonometric functions. Instead, we use Eqs. 15 and 21 and use the real Gaunt coefficients (see Appendix A) to evaluate the products of spherical harmonics. We find that

$$|\mathbf{E}_{\mathrm{ff}}^{(p)}(\theta, \phi, \phi_{\mathrm{pol}}) \cdot \hat{\mathbf{s}}_o|^2 \propto \left[1 + \theta^2 \cos^2(\phi - \phi_{\mathrm{pol}})\right] y_0^0(\hat{\mathbf{s}}_o) + \frac{1}{\sqrt{5}} \left[-1 + 2\theta^2 \cos^2(\phi - \phi_{\mathrm{pol}})\right] y_2^0(\hat{\mathbf{s}}_o) +$$

$$\frac{\sqrt{15}}{10} \theta \sin \phi_{\mathrm{pol}} \cos(\phi - \phi_{\mathrm{pol}}) y_2^{-1}(\hat{\mathbf{s}}_o) + \frac{\sqrt{15}}{10} \theta \cos \phi_{\mathrm{pol}} \cos(\phi - \phi_{\mathrm{pol}}) y_2^1(\hat{\mathbf{s}}_o) -$$

$$\frac{\sqrt{15}}{20} \sin(2\phi_{\mathrm{pol}}) y_2^{-2}(\hat{\mathbf{s}}_o) - \frac{\sqrt{15}}{20} \cos(2\phi_{\mathrm{pol}}) y_2^2(\hat{\mathbf{s}}_o). \tag{22}$$

To find the complete excitation kernel we need to integrate Eq. 22 over all polarization orientations and rays

$$h_{\mathrm{exc}}(\hat{\mathbf{s}}_o) \propto \int_0^\alpha \theta d\theta \int_0^{2\pi} d\phi \int_0^{2\pi} d\phi_{\mathrm{pol}} \, |\mathbf{E}_{\mathrm{ff}}^{(p)} \cdot \hat{\mathbf{s}}_o|^2, \tag{23}$$

where α is the maximum angle the illumination rays make with the optical axis (α is equivalent to the numerical aperture in the paraxial approximation).

After plugging Eq. 22 into Eq. 23 and evaluating the integrals, all but two terms disappear and the excitation kernel is given by

$$h_{\mathrm{exc}}(\hat{\mathbf{s}}_o) \propto \left[1 + \frac{\alpha^2}{4}\right] y_0^0(\hat{\mathbf{s}}_o) + \frac{1}{\sqrt{5}} \left[-1 + \frac{\alpha^2}{2}\right] y_2^0(\hat{\mathbf{s}}_o). \tag{24}$$

We note that the excitation kernel depends on the orientation of the molecule, but it does not depend on the position of the molecule in the focal plane. This is a direct consequence of our illumination geometry—we have placed incoherent light sources in the back focal plane of the objective so each point in the focal plane within the field of view is illuminated equally.

Equation 24 only contains $m = 0$ spherical harmonics, so it can be written as a function of ϑ only. After plugging in the spherical harmonic functions and simplifying we see that

$$h_{\mathrm{exc}}(\vartheta) \propto \sin^2 \vartheta + \frac{1}{2}\alpha^2 \cos^2 \vartheta \tag{25}$$

Equation 24 shows the probability of excitation as a function of dipole orientation and numerical aperture.

2.2.2. Dipole detection model

In this section we will calculate the detection kernel of an epi-detection microscope—the irradiance on the detector due to single molecule at a known position with known orientation. Our approach mimics existing work [1, 8, 9], but we restrict ourselves to the paraxial approximation.

We consider a single dipole emitter at the origin with a fixed dipole emission moment oriented along $\hat{\mathbf{s}}_o$. The electric field at a position $\mathbf{r}$ far from the dipole is given by

$$\mathbf{E}_{\mathrm{ff}}(\mathbf{r}, \hat{\mathbf{s}}_o) \propto \frac{\exp[ik|\hat{\mathbf{r}}|]}{|\hat{\mathbf{r}}|} \hat{\mathbf{r}} \times \hat{\mathbf{s}}_o \times \hat{\mathbf{r}}. \tag{26}$$

We place the dipole in the focal plane of the same $4f$ imaging system we considered in the monopole case—see Figure **??**. The dipole emits spherical wavefronts so we can reuse our argument for shift invariance in the monopole section and drop the phase dependence while keeping in mind that $h_{\mathrm{det}}(\mathbf{r}_d, \mathbf{r}_o, \hat{\mathbf{s}}_o) = h_{\mathrm{det}}(\mathbf{r}_d - \mathbf{r}_o, \hat{\mathbf{s}}_o)$.

$$\mathbf{E}_{\mathrm{ff}}(\mathbf{r}, \hat{\mathbf{s}}_o) \propto [\mathbf{I} - \hat{\mathbf{r}}\hat{\mathbf{r}}^\dagger]\hat{\mathbf{s}}_o \tag{27}$$
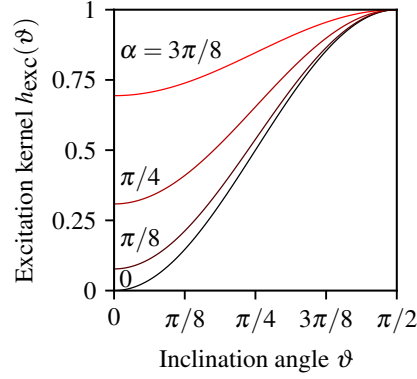
$$\tag{28}$$

Fig. 3. Caption.

$$\hat{\mathbf{r}}(\theta, \phi) \approx \theta \cos \phi \hat{\mathbf{x}} + \theta \sin \phi \hat{\mathbf{y}} + \hat{\mathbf{z}} \tag{29}$$

$$\mathbf{E}_{\text{ff}}(\theta, \phi, \hat{\mathbf{s}}_o) \propto \begin{bmatrix} 1 & 0 & -\theta \cos \phi \\ 0 & 1 & -\theta \sin \phi \\ -\theta \cos \phi & -\theta \sin(\phi) & 0 \end{bmatrix} \hat{\mathbf{s}}_o \tag{30}$$

$$\mathbf{R}_{\text{obj}}(\theta, \phi) = \begin{bmatrix} 1 & 0 & -\theta \cos \phi \\ 0 & 1 & -\theta \sin \phi \\ -\theta \cos \phi & -\theta \sin(\phi) & 1 \end{bmatrix} \tag{31}$$

If we place the molecule in the focal plane of an aplanatic and polarization-preserving objective lens with its optical axis aligned with the $\hat{\mathbf{z}}$ axis (or reuse the illumination objective), then the electric field in the back focal plane of the lens is given by

$$\mathbf{E}_{\text{bfp}}(\theta, \phi, \hat{\mathbf{s}}_o) \propto \mathbf{R}_{\text{obj}}(\theta, \phi)\mathbf{E}_{\text{ff}}(\theta, \phi, \hat{\mathbf{s}}_o) \tag{32}$$

Finally, we change from spherical coordinates to cylindrical coordinates by substituting (r_b, ϕ_b) for (θ, ϕ) and we get

$$\mathbf{E}_{\text{bfp}}(r_b, \phi_b, \hat{\mathbf{s}}_o) \propto \left\{ [s_x - s_z r_b \cos \phi_b] \, \hat{\mathbf{x}} + [s_y - s_z r_b \sin \phi_b] \, \hat{\mathbf{y}} \right\} \Pi \left(\frac{r_b}{\alpha} \right). \tag{33}$$

$$\mathbf{E}_{\text{bfp}}(r_b, \phi_b, \hat{\mathbf{s}}_o) \propto \left\{ s_x \hat{\mathbf{x}} + s_y \hat{\mathbf{y}} + s_z r_b \hat{\boldsymbol{\rho}} \right\} \Pi \left(\frac{r_b}{\alpha} \right). \tag{34}$$

We note that Eq. 33 is identical to previously derived models [Piestun, Backer] except here we have used the paraxial approximation and used spherical harmonic functions.

Next we place a tube lens one focal length from the back focal plane and a detector (see Figure XX)). Under the paraxial approximation we can find the electric field in the detector plane by taking the Fourier transform of the field in the back focal plane [Goodman]

$$\mathbf{E}_{\text{det}}^{(p)}(\mathbf{r}_d, \hat{\mathbf{s}}_o) = \int_{\mathbb{R}^2} d\mathbf{r}_b \mathbf{E}_{\text{bfp}}^{(p)}(\mathbf{r}_b) \exp \left[ik \, \mathbf{r}_b \cdot \mathbf{r}_d \right]. \tag{35}$$

To evaluate the integral we rewrite it in polar coordinates

$$\mathbf{E}_{\text{det}}^{(p)}(\mathbf{r}_d, \hat{\mathbf{s}}_o) = \int_0^\alpha r_b \, dr_b \int_0^{2\pi} d\phi_b \, \mathbf{E}_{\text{bfp}}^{(p)}(r_b, \phi_b) \exp\left[ikr_b r_d \cos(\phi_b - \phi_d)\right], \tag{36}$$

substitute Eq. 33, and apply the following identities

$$\int_0^{2\pi} d\phi_b \left\{ \begin{matrix} \sin(n\phi_b) \\ \cos(n\phi_b) \end{matrix} \right\} \exp\left[ikr_b r_d \cos(\phi_b - \phi_d)\right] = 2\pi i^n \left\{ \begin{matrix} \sin(n\phi_o') \\ \cos(n\phi_o') \end{matrix} \right\} J_n(kr_b r_d), \tag{37}$$

$$\int_0^\alpha dr_b (r_b)^{n+1} J_n(kr_b r_d) = \alpha^{n+1} \left[\frac{J_{n+1}(k\alpha r_d)}{kr_d} \right], \tag{38}$$

to find that

$$\mathbf{E}_{\text{det}}^{(p)}(\mathbf{r}_d, \hat{\mathbf{s}}_o) \propto \left[\frac{J_1(k\alpha r_d)}{k\alpha r_d} y_1^1(\hat{\mathbf{s}}_o) - i\alpha \frac{J_2(k\alpha r_d)}{k\alpha r_d} \cos\phi_d y_1^0(\hat{\mathbf{s}}_o) \right] \hat{\mathbf{x}} +$$
$$\left[\frac{J_1(k\alpha r_d)}{k\alpha r_d} y_1^{-1}(\hat{\mathbf{s}}_o) - i\alpha \frac{J_2(k\alpha r_d)}{k\alpha r_d} \sin\phi_d y_1^0(\hat{\mathbf{s}}_o) \right] \hat{\mathbf{y}}. \tag{39}$$

We can find the irradiance on the detector by taking the modulus squared of the electric field

$$h_{\text{det}}(\mathbf{r}_d, \hat{\mathbf{s}}_o) \propto |\mathbf{E}_{\text{det}}^{(p)}(\mathbf{r}_d, \hat{\mathbf{s}}_o)|^2. \tag{40}$$

We use the real Gaunt coefficients to find that

$$h_{\text{det}}(\mathbf{r}_d, \hat{\mathbf{s}}_o) \propto \left[a_1(r_d) + \frac{\alpha^2}{4} a_2(r_d) \right] y_0^0(\hat{\mathbf{s}}_o) + \frac{1}{\sqrt{5}} \left[-a_1(r_d) + \frac{\alpha^2}{2} a_2(r_d) \right] y_2^0(\hat{\mathbf{s}}_o), \tag{41}$$

where we have defined

$$a_n(r_d) \equiv \frac{n}{\pi} \left[\frac{J_n(k\alpha r_d)}{k\alpha r_d} \right]^2. \tag{42}$$

Similar to the excitation kernel, we can write the excitation kernel purely in terms of the inclination angle

$$h_{\text{det}}(r_d, \vartheta) \propto a_1(r_d) \sin^2\vartheta + \frac{1}{2}\alpha^2 a_2(r_d) \cos^2(\vartheta). \tag{43}$$

In our analysis we have only considered a dipole radiator at the origin, but we can use the shift-invariance of $4f$ imaging systems to model dipole radiators at arbitrary positions in the focal plane. If we shift the dipole radiator to an in-focus position $\mathbf{r}_o$, then the irradiance pattern on the detector will be given by $h_{\text{det}}(\mathbf{r}_d - \mathbf{r}_o)$. We have also restricted our analysis to an imaging system with unit magnification, but an imaging system with an arbitrary magnification can be modeled as a system with unit magnification using a change of variables (see [10] section 7.2.7).

Finally, we note the similarities between Eqs. 24 and 41. If we integrate the detection kernel over the detector and use the identity $\int_{\mathbb{R}^2} d\mathbf{r} \, a_n(r) = 1$ for $n \in \mathbb{N}$, then we find that the excitation and detection kernels are related by

$$h_{\text{exc}}(\hat{\mathbf{s}}_o) = \int_{\mathbb{R}^2} d\mathbf{r} h_{\text{det}}(\mathbf{r}, \hat{\mathbf{s}}_o). \tag{44}$$
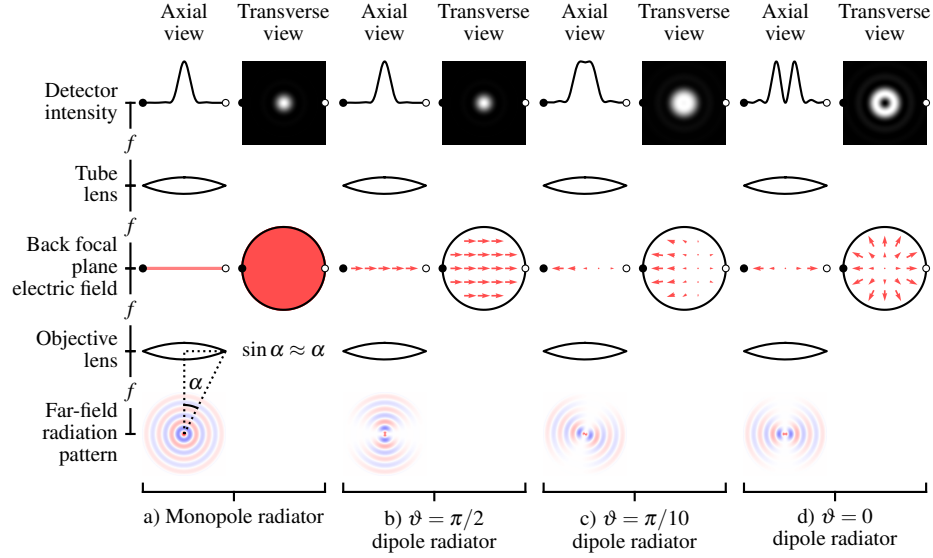
Fig. 4. Comparison of paraxial detection models for monopole radiators a) and dipole radiators b)–d). Monopole radiators fill the back focal plane with a uniform scalar field which gives rise to the familiar Airy disk on the detector. A transverse dipole radiator also creates an Airy disk—the back focal plane is filled with a uniform vector field. An axial dipole radiator creates a radial electric field pattern in the back focal plane which gives rise to a higher-order Airy disk. Back focal plane electric fields from transverse dipoles are purely even while fields from axial dipoles are purely odd which causes a relative $\pi/2$ phase shift for the fields on the detector. The back focal plane fields from an arbitrarily-oriented dipole can be decomposed into even and odd fields, so the final intensity pattern is always radially symmetric.

2.3. Spatio-angular transfer function

$$g(\mathbf{r}_d) = \int_{\mathbb{S}^2} d\hat{\mathbf{s}}_o \int_{\mathbb{R}^2} d\mathbf{r}_o\, h(|\mathbf{r}_d - \mathbf{r}_o|, \hat{\mathbf{s}}_o) f(\mathbf{r}_o, \hat{\mathbf{s}}_o). \tag{45}$$

$$g(\mathbf{r}_d) = \mathcal{F}_{\mathbb{R}^2}^{-1}\left\{ \int_{\mathbb{S}^2} d\hat{\mathbf{s}}_o\, \mathcal{F}_{\mathbb{R}^2}\left\{ h(|\mathbf{r}_d - \mathbf{r}_o|, \hat{\mathbf{s}}_o) \right\} \mathcal{F}_{\mathbb{R}^2}\left\{ f(\mathbf{r}_o, \hat{\mathbf{s}}_o) \right\} \right\}. \tag{46}$$

$$\int_{\mathbb{S}^2} d\hat{\mathbf{s}}\, f(\hat{\mathbf{s}})g(\hat{\mathbf{s}}) = \sum_{l=0}^{\infty} \sum_{m=-l}^{l} \mathcal{F}_{\mathbb{S}^2}\left\{ f(\hat{\mathbf{s}}) \right\} \mathcal{F}_{\mathbb{S}^2}\left\{ g(\hat{\mathbf{s}}) \right\}, \tag{47}$$

where

$$\mathcal{F}_{\mathbb{S}^2}\left\{ f(\hat{\mathbf{s}}) \right\} \equiv \int_{\mathbb{S}^2} f(\hat{\mathbf{s}}) y_l^m(\hat{\mathbf{s}}). \tag{48}$$

Eq. 47 is the generalized Plancharel theorem for spherical functions. It is a special case of the fact that scalar products are invariant under unitary transformations (see Barrett 3.78). Next, we plug Eq. 47 into Eq. **??** to get

$$g(\mathbf{r}_d) = \mathcal{F}_{\mathbb{R}^2}^{-1}\left\{ \sum_{l=0}^{\infty} \sum_{m=-l}^{l} H_l^m(\nu, \hat{\mathbf{p}}) \mathcal{F}_{\mathbb{R}^2 \times \mathbb{S}^2}\left\{ f(\mathbf{r}_o, \hat{\mathbf{s}}_o) \right\} \right\} \tag{49}$$
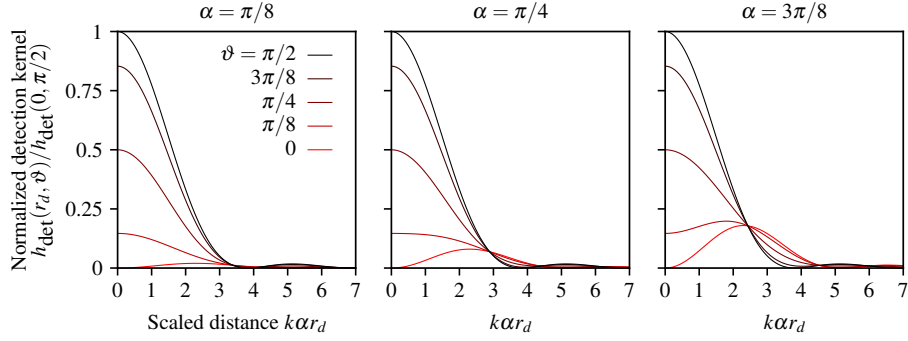
Fig. 5. Normalized detection kernel as a function of the scaled radial detection coordinate $k\alpha r_d$, the dipole inclination angle ϑ, and the collection angle α. For small collection angles (left) the detection kernel of axial dipoles (**red**) is small compared to transverse dipoles (**black**), but the relative contribution of axial dipoles increases with the collection angle (see **red** lines from left to right).

where

$$H_l^m(\boldsymbol{\nu}) \equiv \mathcal{F}_{\mathbb{R}^2 \times \mathbb{S}^2} \{h(|\mathbf{r}_d - \mathbf{r}_o|, \hat{\mathbf{s}}_o)\} \equiv \int_{\mathbb{R}^3} d\mathbf{r}_o \, e^{i2\pi \mathbf{r}_o \cdot \boldsymbol{\nu}} \int_{\mathbb{S}^2} d\hat{\mathbf{s}}_o \, y_l^m(\hat{\mathbf{s}}_o) h(\mathbf{r}_o, \hat{\mathbf{s}}_o). \tag{50}$$

Eq. 49 is the main result of this section. Right now it is not obvious that Eq. 49 is any more efficient than Eq. **??**, but when we calculate the transfer function we will see that the sum over spherical harmonics contains a small number of terms.

As written Eq. **??** is an extremely expensive integral to compute—to find the irradiance at a single point on the detector we need to evaluate the spatio-angular density and the kernel at every point in $\mathbb{S}^2 \times \mathbb{R}^2$. To simplify the integral, we expand the object and the kernel onto complex exponentials and spherical harmonics using

$$F_l^m(\boldsymbol{\nu}) \equiv \int_{\mathbb{S}^2} d\hat{\mathbf{s}}_o \, y_l^m(\hat{\mathbf{s}}_o) \int_{\mathbb{R}^2} d\mathbf{r}_o \exp\left[i2\pi \mathbf{r}_o \cdot \boldsymbol{\nu}\right] f(\mathbf{r}_o, \hat{\mathbf{s}}_o), \tag{51}$$

$$H_l^m(\boldsymbol{\nu}) \equiv \int_{\mathbb{S}^2} d\hat{\mathbf{s}}_o \, y_l^m(\hat{\mathbf{s}}_o) \int_{\mathbb{R}^2} d\mathbf{r}_o \exp\left[i2\pi \mathbf{r}_o \cdot \boldsymbol{\nu}\right] h(\mathbf{r}_o, \hat{\mathbf{s}}_o). \tag{52}$$

We also expand the detector irradiance onto spatial harmonics using the Fourier transform

$$G(\boldsymbol{\nu}) \equiv \int_{\mathbb{R}^2} d\mathbf{r}_d \exp\left[i2\pi \mathbf{r}_d \cdot \boldsymbol{\nu}\right] g(\mathbf{r}_d). \tag{53}$$

Given these definitions, we can rewrite Eq. **??** in the frequency domain as

$$G(\boldsymbol{\nu}) = \sum_{l=0}^{\infty} \sum_{m=-l}^{l} H_l^m(\boldsymbol{\nu}) F_l^m(\boldsymbol{\nu}). \tag{54}$$

In Appendix A we calculate the spatio-angular transfer function as

$$H_l^m(\nu) = \frac{1}{C}\left\{ \left[\left(1 + \frac{\alpha^2}{8}\right) A_1(\nu) + \left(\frac{\alpha^2}{8} + \frac{3\alpha^4}{32}\right) A_2(\nu)\right] \delta_{l0}\delta_{m0} + \right.$$
$$\frac{2\sqrt{5}}{7}\left[\left(-1 + \frac{\alpha^2}{16}\right) A_1(\nu) + \left(\frac{\alpha^2}{16} + \frac{3\alpha^4}{16}\right) A_2(\nu)\right] \delta_{l2}\delta_{m0}$$
$$\left. \frac{1}{7}\left[\left(1 - \frac{\alpha^2}{2}\right) A_1(\nu) + \left(-\frac{\alpha^2}{2} + \frac{\alpha^4}{4}\right) A_2(\nu)\right] \delta_{l4}\delta_{m0}\right\}, \tag{55}$$

where

$$A_1(\nu) = \frac{2}{\pi}\left\{\cos^{-1}\left(\frac{\nu}{2\nu_o}\right) - \frac{\nu}{2\nu_o}\sqrt{1 - \left(\frac{\nu}{2\nu_o}\right)^2}\right\} \Pi\left(\frac{\nu}{2\nu_o}\right), \tag{56}$$

$$A_2(\nu) = \frac{2}{\pi}\left\{\cos^{-1}\left(\frac{\nu}{2\nu_o}\right) - \left[3 - 2\left(\frac{\nu}{2\nu_o}\right)^2\right]\frac{\nu}{2\nu_o}\sqrt{1 - \left(\frac{\nu}{2\nu_o}\right)^2}\right\}\Pi\left(\frac{\nu}{2\nu_o}\right), \tag{57}$$

and $C = 1 + \frac{\alpha^2}{4} + \frac{3\alpha^4}{32}$ is a normalization constant.

3. Results

4. Discussion and conclusion

Do microscopes transmit more information than Abbe thought?

Using an experimentally determined model is an effective way to find an accurate model without understanding all of the physical details of the imaging system, but these approaches require a known input that can completely characterize the imaging system. Sub-diffraction beads are commonly used as a known input for measuring the response of a microscope, but we argue that sub-diffraction beads are not enough to completely characterize the response of a microscope to all fluorescent samples. Beads can only characterize the response of the microscope to an angularly uniform distribution of fluorophores, and we will show that all microscopes have an orientation-dependent response. A complete characterization requires a test sample with at least three known orientation distributions.

Can experimentally measured psfs account for this?

References

1. A. S. Backer and W. E. Moerner, "Extending single-molecule microscopy using optical Fourier processing," J. Phys. Chem. B **118**, 8313–8329 (2014).
2. M. A. Lieb, J. M. Zavislan, and L. Novotny, "Single-molecule orientations determined by direct emission pattern imaging," J. Opt. Soc. Am. B **21**, 1210–1215 (2004).
3. M. P. Backlund, M. D. Lew, A. S. Backer, S. J. Sahl, and W. E. Moerner, "The role of molecular dipole orientation in single-molecule fluorescence microscopy and implications for super-resolution imaging," ChemPhysChem **15**, 587–599 (2014).
4. S. B. Mehta, M. McQuilken, P. J. La Rivière, P. Occhipinti, A. Verma, R. Oldenbourg, A. S. Gladfelter, and T. Tani, "Dissection of molecular assembly dynamics by tracking orientation and position of single molecules in live cells," Proc. Natl. Acad. Sci. U.S.A. **113**, E6352–E6361 (2016).
5. J. Goodman, *Introduction to Fourier Optics* (McGraw-Hill, 1996), 2nd ed.
6. J. T. Fourkas, "Rapid determination of the three-dimensional orientation of single molecules," Opt. Lett. **26**, 211–213 (2001).
7. T. Chandler, S. Mehta, H. Shroff, R. Oldenbourg, and P. J. La Rivière, "Single-fluorophore orientation determination with multiview polarized illumination: modeling and microscope design," Opt. Express **25**, 31309–31325 (2017).
8. L. Novotny and B. Hecht, *Principles of Nano-Optics* (Cambridge University Press, 2006).
9. A. Agrawal, S. Quirin, G. Grover, and R. Piestun, "Limits of 3D dipole localization and orientation estimation for single-molecule imaging: towards Green's tensor engineering," Opt. Express **20**, 26667–26680 (2012).

10. H. Barrett and K. Myers, *Foundations of image science*, Wiley series in pure and applied optics (Wiley-Interscience, 2004).
11. J. Mertz, *Introduction to Optical Microscopy* (W. H. Freeman, 2009).
12. A. Poularikas, *Handbook of Formulas and Tables for Signal Processing*, Electrical Engineering Handbook (CRC-Press, 1998).

A. Spherical harmonics

The spherical harmonics are a basis for representing functions on the sphere. In this appendix we will define the basis and review several important properties of this set of functions.

The complex-valued spherical harmonics are given by

$$Y_l^m(\vartheta, \varphi) = \sqrt{\frac{(2l + 1)(l - m)!}{4\pi(l + m)!}} \exp(im\varphi)P_l^m(\cos\theta) \tag{58}$$

where $P_l^m(\cos\theta)$ are the associated Legendre polynomials that include the Condon-Shortley phase. In this work we only use the spherical harmonics to represent real-valued functions so we use the real spherical harmonics given by

$$y_l^m(\vartheta, \varphi) \begin{cases} \frac{Y_l^m(\vartheta,\varphi)+(-1)^m Y_l^{-m}(\vartheta,\varphi)}{\sqrt{2}} & m > 0, \\ Y_l^m(\vartheta, \varphi) & m = 0, \\ \frac{Y_l^m(\vartheta,\varphi)-(-1)^m Y_l^{-m}(\vartheta,\varphi)}{i\sqrt{2}} & m < 0. \end{cases} \tag{59}$$

The $l = 0, 1, 2$ spherical harmonics are given by

$$y_0^0(\vartheta, \varphi) = \sqrt{\frac{1}{4\pi}},$$

$$y_1^{-1}(\vartheta, \varphi) = \sqrt{\frac{3}{4\pi}} \sin\varphi \sin\vartheta,$$

$$y_1^0(\vartheta, \varphi) = \sqrt{\frac{3}{4\pi}} \cos\vartheta,$$

$$y_1^1(\vartheta, \varphi) = \sqrt{\frac{3}{4\pi}} \cos\varphi \sin\vartheta,$$

$$y_2^{-2}(\vartheta, \varphi) = \sqrt{\frac{15}{4\pi}} \sin\varphi \cos\varphi \sin^2\vartheta,$$

$$y_2^{-1}(\vartheta, \varphi) = \sqrt{\frac{15}{4\pi}} \sin\varphi \sin\vartheta \cos\vartheta,$$

$$y_2^0(\vartheta, \varphi) = \sqrt{\frac{5}{16\pi}}(3\cos^2\vartheta - 1),$$

$$y_2^1(\vartheta, \varphi) = \sqrt{\frac{15}{4\pi}} \cos\varphi \sin\vartheta \cos\vartheta,$$

$$y_2^2(\vartheta, \varphi) = \sqrt{\frac{15}{16\pi}}(\cos^2\varphi - \sin^2\varphi)\sin^2\vartheta. \tag{60}$$

Real Gaunt coefficients

B. Evaluating the spatio-angular transfer function

In this appendix we will evaluate

$$H_l^m(\nu) \propto \int_{\mathbb{S}^2} d\hat{\mathbf{s}}_o y_l^m(\hat{\mathbf{s}}_o) \int_{\mathbb{R}^2} d\mathbf{r}_o \exp\left[i2\pi\mathbf{r}_o \cdot \nu\right] h(\mathbf{r}_o, \hat{\mathbf{s}}_o), \tag{61}$$

where

$$h(\mathbf{r}_d - \mathbf{r}_o, \hat{\mathbf{s}}_o) \propto h_{\text{exc}}(\hat{\mathbf{s}}_o) h_{\text{det}}(\mathbf{r}_d - \mathbf{r}_o, \hat{\mathbf{s}}_o), \tag{62}$$

$$h_{\text{exc}}(\hat{\mathbf{s}}_o) \propto \left[1 + \frac{\alpha^2}{4}\right] y_0^0(\hat{\mathbf{s}}_o) + \frac{1}{\sqrt{5}}\left[-1 + \frac{\alpha^2}{2}\right] y_2^0(\hat{\mathbf{s}}_o), \tag{63}$$

$$h_{\text{det}}(\mathbf{r}_d, \hat{\mathbf{s}}_o) \propto \left[a_1(r_d) + \frac{\alpha^2}{4}a_2(r_d)\right] y_0^0(\hat{\mathbf{s}}_o) + \frac{1}{\sqrt{5}}\left[-a_1(r_d) + \frac{\alpha^2}{2}a_2(r_d)\right] y_2^0(\hat{\mathbf{s}}_o), \tag{64}$$

and

$$a_n(r_d) \equiv \frac{n}{\pi}\left[\frac{J_n(k\alpha r_d)}{k\alpha r_d}\right]^2. \tag{65}$$

First we plug Eq. 62 into Eq. 61 and move the excitation kernel out of the spatial integral

$$H_l^m(\mathbf{v}) \propto \int_{\mathbb{S}^2} d\hat{\mathbf{s}}_o\, y_l^m(\hat{\mathbf{s}}_o) h_{\text{exc}}(\hat{\mathbf{s}}_o) \int_{\mathbb{R}^2} d\mathbf{r}_o\, \exp\left[i2\pi \mathbf{r}_o \cdot \mathbf{v}\right] h_{\text{det}}(\mathbf{r}_d, \hat{\mathbf{s}}_o). \tag{66}$$

The spatial integral requires us to evaluate the two-dimensional Fourier transform of $a_1(r_o)$ and $a_2(r_o)$. We will define

$$A_n(\mathbf{v}) \equiv \mathcal{F}_2\{a_n(r_o)\} = \int_{\mathbb{R}^2} d\mathbf{r}_o\, \exp\left[i2\pi \mathbf{r}_o \cdot \mathbf{v}\right] a_n(r_d), \tag{67}$$

and evaluate $A_1(\mathbf{v})$ and $A_2(\mathbf{v})$ later. After substituting 67 into Eq. 66 we find

$$H_l^m(\mathbf{v}) \propto \int_{\mathbb{S}^2} d\hat{\mathbf{s}}_o\, y_l^m(\hat{\mathbf{s}}_o)\left\{\left[1 + \frac{\alpha^2}{4}\right] y_0^0(\hat{\mathbf{s}}_o) + \frac{1}{\sqrt{5}}\left[-1 + \frac{\alpha^2}{2}\right] y_2^0(\hat{\mathbf{s}}_o)\right\} +$$
$$\left\{\left[A_1(\mathbf{v}) + \frac{\alpha^2}{4}A_2(\mathbf{v})\right] y_0^0(\hat{\mathbf{s}}_o) + \frac{1}{\sqrt{5}}\left[-A_1(\mathbf{v}) + \frac{\alpha^2}{2}A_2(\mathbf{v})\right] y_2^0(\hat{\mathbf{s}}_o)\right\}. \tag{68}$$

After expanding the products of spherical harmonics

$$H_l^m(\mathbf{v}) \propto \int_{\mathbb{S}^2} d\hat{\mathbf{s}}_o\, y_l^m(\hat{\mathbf{s}}_o)\left\{\left[\frac{3}{5}A_1(\mathbf{v}) + \frac{3\alpha^2}{40}[A_1(\mathbf{v}) + A_2(\mathbf{v})] + \frac{9\alpha^4}{160}A_2(\mathbf{v})\right] y_0^0(\hat{\mathbf{s}}_o)+\right.$$
$$\frac{3\sqrt{5}}{280}\left[-16A_1(\mathbf{v}) + \alpha^2[A_1(\mathbf{v}) + A_2(\mathbf{v})] + 3\alpha^4 A_2(\mathbf{v})\right] y_2^0(\hat{\mathbf{s}}_o)$$
$$\left.\frac{3}{35}\left[\left(1 - \frac{\alpha^2}{2}\right)A_1(\mathbf{v}) + \left(-\frac{\alpha^2}{2} + \frac{\alpha^4}{4}\right)A_2(\mathbf{v})\right] y_4^0(\hat{\mathbf{s}}_o)\right\}, \tag{69}$$

$$H_l^m(\mathbf{v}) \propto \int_{\mathbb{S}^2} d\hat{\mathbf{s}}_o\, y_l^m(\hat{\mathbf{s}}_o)\left\{\left[\left(1 + \frac{\alpha^2}{8}\right)A_1(\mathbf{v}) + \left(\frac{\alpha^2}{8} + \frac{3\alpha^4}{32}\right)A_2(\mathbf{v})\right] y_0^0(\hat{\mathbf{s}}_o)+\right.$$
$$\frac{\sqrt{5}}{56}\left[(-16 + \alpha^2)A_1(\mathbf{v}) + (\alpha^2 + 3\alpha^4)A_2(\mathbf{v})\right] y_2^0(\hat{\mathbf{s}}_o)$$
$$\left.\frac{1}{7}\left[\left(1 - \frac{\alpha^2}{2}\right)A_1(\mathbf{v}) + \left(-\frac{\alpha^2}{2} + \frac{\alpha^4}{4}\right)A_2(\mathbf{v})\right] y_4^0(\hat{\mathbf{s}}_o)\right\}. \tag{70}$$

Next, we use the orthogonality of spherical harmonics to evaluate the angular integral

$$H_l^m(\nu) = \frac{1}{C} \Bigg\{ \left[\left(1 + \frac{\alpha^2}{8} \right) A_1(\nu) + \left(\frac{\alpha^2}{8} + \frac{3\alpha^4}{32} \right) A_2(\nu) \right] \delta_{l0}\delta_{m0} +$$

$$\frac{2\sqrt{5}}{7} \left[\left(-1 + \frac{\alpha^2}{16} \right) A_1(\nu) + \left(\frac{\alpha^2}{16} + \frac{3\alpha^4}{16} \right) A_2(\nu) \right] \delta_{l2}\delta_{m0}$$

$$\frac{1}{7} \left[\left(1 - \frac{\alpha^2}{2} \right) A_1(\nu) + \left(-\frac{\alpha^2}{2} + \frac{\alpha^4}{4} \right) A_2(\nu) \right] \delta_{l4}\delta_{m0} \Bigg\}, \tag{71}$$

where $C = 1 + \frac{\alpha^2}{4} + \frac{3\alpha^4}{32}$ is a normalization constant.

Our final task is to calculate $A_1(\nu)$ and $A_2(\nu)$. $A_1(\nu)$ is a well-known result [5, 11], but we review the calculation to establish the tools we'll need to evaluate $A_2(\nu)$. We start by using the autocorrelation (Wiener-Khinchin) theorem to rewrite the Fourier transform as

$$A_1(\nu) = \frac{1}{\pi} \mathcal{F}_2 \left\{ \left[\frac{J_1(2\pi\nu_o r_o)}{2\pi\nu_o r_o} \right]^2 \right\} = \frac{1}{\pi} \left[\mathcal{F}_2 \left\{ \frac{J_1(2\pi\nu_o r_o)}{2\pi\nu_o r_o} \right\} \star_2 \mathcal{F}_2 \left\{ \frac{J_1(2\pi\nu_o r_o)}{2\pi\nu_o r_o} \right\} \right] \tag{72}$$

where $\star_2$ denotes a two-dimensional autocorrelation. Next, we recognize that the Fourier transforms on the right hand side of Eq. 72 are rotationally symmetric so they can be rewritten as zero-order Hankel transforms

$$A_1(\nu) = \frac{1}{\pi} \left[\mathcal{H}_0 \left\{ \frac{J_1(2\pi\nu_o r_o)}{2\pi\nu_o r_o} \right\} \star_2 \mathcal{H}_0 \left\{ \frac{J_1(2\pi\nu_o r_o)}{2\pi\nu_o r_o} \right\} \right] \tag{73}$$

We can apply the Hankel transform identity [12]

$$\mathcal{H}_{n-1} \left\{ \frac{J_n(2\pi\nu_o r_o)}{2\pi\nu_o r_o} \right\} = \frac{\nu^{n-1}}{\nu_o^n} \Pi \left(\frac{\nu}{\nu_o} \right), \tag{74}$$

to find that

$$A_1(\nu) = \frac{1}{\pi\nu_o^2} \left[\Pi \left(\frac{\nu}{\nu_o} \right) \star_2 \Pi \left(\frac{\nu}{\nu_o} \right) \right]. \tag{75}$$

We can use the geometric construction in Figure 6 to express the autocorrelation in terms of an integral over a region of overlap between two circles given by

$$A_1(\nu) = \frac{4}{\pi\nu_o^2} \left[\int_0^{\nu_o} \tau d\tau \int_0^{\cos^{-1}\left(\frac{\nu}{2\nu_o} \right)} d\phi_\tau - \int_0^{\nu/2} d\tau_x \int_0^{\tau_x \frac{2\nu_o}{\nu} \sqrt{1 - \left(\frac{\nu}{2\nu_o} \right)^2}} d\tau_y \right] \Pi \left(\frac{\nu}{2\nu_o} \right), \tag{76}$$

$$A_1(\nu) = \frac{4}{\pi\nu_o^2} \left[\int_0^{\nu_o} \tau d\tau \cos^{-1} \left(\frac{\nu}{2\nu_o} \right) - \int_0^{\nu/2} d\tau_x \tau_x \frac{2\nu_o}{\nu} \sqrt{1 - \left(\frac{\nu}{2\nu_o} \right)^2} \right] \Pi \left(\frac{\nu}{2\nu_o} \right), \tag{77}$$

$$A_1(\nu) = \frac{2}{\pi} \left\{ \cos^{-1} \left(\frac{\nu}{2\nu_o} \right) - \frac{\nu}{2\nu_o} \sqrt{1 - \left(\frac{\nu}{2\nu_o} \right)^2} \right\} \Pi \left(\frac{\nu}{2\nu_o} \right). \tag{78}$$

To evaluate $A_2(\nu)$ we could follow the same steps, but we will reach a dead end because there is no Hankel transform identity for $\mathcal{H}_{n-1} \left\{ \frac{J_{n+1}(2\pi\nu_o r_o)}{2\pi\nu_o r_o} \right\}$. Instead, we rewrite $A_2(\nu)$ as

$$A_2(\nu) = \frac{2}{\pi} \mathcal{F}_2 \left\{ \left[\frac{J_2(2\pi\nu_o r_o)}{2\pi\nu_o r_o} \right]^2 \right\} = \frac{2}{\pi} \left[\mathcal{F}_2 \left\{ \left[\frac{J_2(2\pi\nu_o r_o)}{2\pi\nu_o r_o} \cos \phi_\nu \right]^2 \right\} + \mathcal{F}_2 \left\{ \left[\frac{J_2(2\pi\nu_o r_o)}{2\pi\nu_o r_o} \sin \phi_\nu \right]^2 \right\} \right]. \tag{79}$$
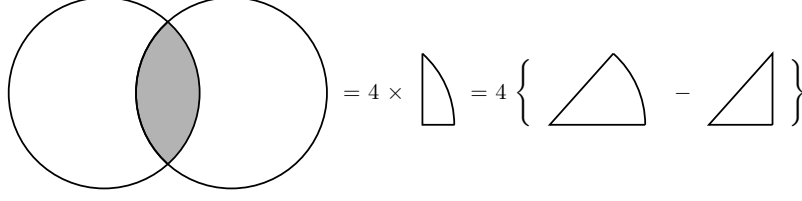
Fig. 6. Geometric construction for evaluating the autocorrelations. We need to integrate over the overlapping region of two circles with radius ν_o and distance ν between their centers. The region is given by four times the difference in area between a sector of angle $\arccos\left(\frac{\nu}{2\nu_o}\right)$ and a triangle with base $\nu/2$ and hypotenuse ν_o.

Applying the autocorrelation theorem gives

$$A_2(\nu) = \frac{2}{\pi}\left[\mathcal{F}_2\left\{\frac{J_2(2\pi\nu_o r_o)}{2\pi\nu_o r_o}\cos\phi_\nu\right\} \star_2 \mathcal{F}_2\left\{\frac{J_2(2\pi\nu_o r_o)}{2\pi\nu_o r_o}\cos\phi_\nu\right\} + \right.$$

$$\left. \mathcal{F}_2\left\{\frac{J_2(2\pi\nu_o r_o)}{2\pi\nu_o r_o}\sin\phi_\nu\right\} \star_2 \mathcal{F}_2\left\{\frac{J_2(2\pi\nu_o r_o)}{2\pi\nu_o r_o}\sin\phi_\nu\right\}\right]. \tag{80}$$

After converting the Fourier transforms to Hankel transforms with the identities

$$\mathcal{F}_2\left\{f(r)\cos(\phi)\right\} = -i\cos\phi_\nu\mathcal{H}_1\left\{f(r)\right\}, \tag{81}$$

$$\mathcal{F}_2\left\{f(r)\sin(\phi)\right\} = -i\sin\phi_\nu\mathcal{H}_1\left\{f(r)\right\}, \tag{82}$$

and evaluating the Hankel transforms with Eq. 74, we find that

$$A_2(\nu) = -\frac{2}{\pi\nu_o^4}\left\{\left[\nu_x\Pi\left(\frac{\nu}{\nu_o}\right)\star_2\nu_x\Pi\left(\frac{\nu}{\nu_o}\right)\right] + \left[\nu_y\Pi\left(\frac{\nu}{\nu_o}\right)\star_2\nu_y\Pi\left(\frac{\nu}{\nu_o}\right)\right]\right\}. \tag{83}$$

Eq. 83 contains two autocorrelations that require us to find the weighted overlap of two circles. Neither of these autocorrelations are rotationally symmetric, but their sum must be rotationally symmetric. With this symmetry in mind, we recognize that the first autocorrelation is largest for shifts along the x direction and smallest for shifts along the y direction with a smooth $\cos^2\phi_\nu$ weighting between the two extremes. The same is true for the second autocorrelations except the x and y axes are exchanged and there is a $\sin^2\phi_\nu$ weighting between the two extremes. Therefore, we can rewrite Eq. 83 as

$$A_2(\nu) = -\frac{2}{\pi\nu_o^4}\left\{\left[\nu_x\Pi\left(\frac{\nu}{\nu_o}\right)\star_2^x\nu_x\Pi\left(\frac{\nu}{\nu_o}\right)\right]\cos^2\phi_\nu + \left[\nu_x\Pi\left(\frac{\nu}{\nu_o}\right)\star_2^y\nu_x\Pi\left(\frac{\nu}{\nu_o}\right)\right]\sin^2\phi_\nu + \right.$$

$$\left. \left[\nu_y\Pi\left(\frac{\nu}{\nu_o}\right)\star_2^x\nu_y\Pi\left(\frac{\nu}{\nu_o}\right)\right]\cos^2\phi_\nu + \left[\nu_y\Pi\left(\frac{\nu}{\nu_o}\right)\star_2^y\nu_y\Pi\left(\frac{\nu}{\nu_o}\right)\right]\sin^2\phi_\nu\right\}. \tag{84}$$

where $\star_2^x$ denotes a two-dimensional autocorrelation for shifts along the x direction. We can use the following pair of identities

$$\nu_x\Pi\left(\frac{\nu}{\nu_o}\right)\star_2^x\nu_x\Pi\left(\frac{\nu}{\nu_o}\right) = \nu_y\Pi\left(\frac{\nu}{\nu_o}\right)\star_2^y\nu_y\Pi\left(\frac{\nu}{\nu_o}\right), \tag{85}$$

$$\nu_x\Pi\left(\frac{\nu}{\nu_o}\right)\star_2^y\nu_x\Pi\left(\frac{\nu}{\nu_o}\right) = \nu_y\Pi\left(\frac{\nu}{\nu_o}\right)\star_2^x\nu_y\Pi\left(\frac{\nu}{\nu_o}\right), \tag{86}$$

to simplify Eq. 84 to

$$A_2(\nu) = -\frac{2}{\pi \nu_o^4} \left\{ \left[\nu_x \Pi \left(\frac{\nu}{\nu_o} \right) \star_2^x \nu_x \Pi \left(\frac{\nu}{\nu_o} \right) \right] + \left[\nu_x \Pi \left(\frac{\nu}{\nu_o} \right) \star_2^y \nu_x \Pi \left(\frac{\nu}{\nu_o} \right) \right] \right\}. \qquad (87)$$

First we evaluate the autocorrelation for shifts along the x axis

$$= -\frac{2}{\pi \nu_o^4} \left[\nu_x \Pi \left(\frac{\nu}{\nu_o} \right) \star_2^x \nu_x \Pi \left(\frac{\nu}{\nu_o} \right) \right] \qquad (88)$$

$$= -\frac{8}{\pi \nu_o^4} \left[\int_0^{\nu_o} \tau \, d\tau \int_0^{\cos^{-1}\left(\frac{\nu}{2\nu_o} \right)} d\phi_\tau (-\tau^2 \cos^2 \phi_\tau + \nu \tau \cos \phi_\tau) \right. \qquad (89)$$

$$\left. - \int_0^{\nu/2} d\tau_x \int_0^{\tau_x \frac{2\nu_o}{\nu} \sqrt{1 - \left(\frac{\nu}{2\nu_o} \right)^2}} d\tau_y (-\tau_x^2 + \nu \tau_x) \right] \Pi \left(\frac{\nu}{2\nu_o} \right). \qquad (90)$$

For the first inner integral we make use of the following identities

$$\int_0^{\cos^{-1} z} d\phi \cos^2 \phi = \frac{1}{2} z \sqrt{1 - z^2} + \frac{1}{2} \cos^{-1} z, \qquad (91)$$

$$\int_0^{\cos^{-1} z} d\phi \cos \phi = \sqrt{1 - z^2}, \qquad (92)$$

which results in

$$= -\frac{8}{\pi \nu_o^4} \left[\int_0^{\nu_o} d\tau \frac{-\tau^3}{2} \left(\frac{\nu}{2\nu_o} \sqrt{1 - \left(\frac{\nu}{2\nu_o} \right)^2} + \cos^{-1} \left(\frac{\nu}{2\nu_o} \right) \right) + \nu \tau^2 \sqrt{1 - \left(\frac{\nu}{2\nu_o} \right)^2} \right. $$
$$\left. \int_0^{\nu/2} d\tau_x \int_0^{\tau_x \frac{2\nu_o}{\nu} \sqrt{1 - \left(\frac{\nu}{2\nu_o} \right)^2}} d\tau_y (-\tau_x^2 + \nu \tau_x) \right] \Pi \left(\frac{\nu}{2\nu_o} \right), \qquad (93)$$

$$= -\frac{8}{\pi \nu_o^4} \left[\frac{-\nu_o^4}{8} \left(\frac{\nu}{2\nu_o} \sqrt{1 - \left(\frac{\nu}{2\nu_o} \right)^2} + \arccos \left(\frac{\nu}{2\nu_o} \right) \right) + \frac{2\nu_o^4}{3} \frac{\nu}{2\nu_o} \sqrt{1 - \left(\frac{\nu}{2\nu_o} \right)^2} \right. $$
$$\left. - \frac{5\nu^2 \nu_o^2}{48} \frac{\nu}{2\nu_o} \sqrt{1 - \left(\frac{\nu}{2\nu_o} \right)^2} \right] \Pi \left(\frac{\nu}{2\nu_o} \right), \qquad (94)$$

$$= \frac{1}{\pi} \left[\left(\frac{\nu}{2\nu_o} \sqrt{1 - \left(\frac{\nu}{2\nu_o} \right)^2} + \arccos \left(\frac{\nu}{2\nu_o} \right) \right) - \frac{16}{3} \frac{\nu}{2\nu_o} \sqrt{1 - \left(\frac{\nu}{2\nu_o} \right)^2} \right. $$
$$\left. + \frac{5\nu^2}{6\nu_o^2} \frac{\nu}{2\nu_o} \sqrt{1 - \left(\frac{\nu}{2\nu_o} \right)^2} \right] \Pi \left(\frac{\nu}{2\nu_o} \right), \qquad (95)$$

$$= \frac{1}{\pi} \left[\arccos \left(\frac{\nu}{2\nu_o} \right) - \left(\frac{13}{3} - \frac{5\nu^2}{6\nu_o^2} \right) \frac{\nu}{2\nu_o} \sqrt{1 - \left(\frac{\nu}{2\nu_o} \right)^2} \right] \Pi \left(\frac{\nu}{2\nu_o} \right), \qquad (96)$$

$$= \frac{1}{\pi} \left[\arccos \left(\frac{\nu}{2\nu_o} \right) - \frac{1}{3} \left[13 - 10 \left(\frac{\nu}{2\nu_o} \right)^2 \right] \frac{\nu}{2\nu_o} \sqrt{1 - \left(\frac{\nu}{2\nu_o} \right)^2} \right] \Pi \left(\frac{\nu}{2\nu_o} \right). \qquad (97)$$

Next we evaluate the autocorrelation for shifts along the y axis

$$\frac{-2}{\pi v_0^4}\left\{\left[v_x\,\Pi\left(\frac{v}{v_o}\right)\right]\star_2^y\left[v_x\,\Pi\left(\frac{v}{v_o}\right)\right]\right\}= \tag{98}$$

$$=\frac{-8}{\pi v_o^4}\left[\int_0^{v_o}d\tau\,\tau\int_0^{\cos^{-1}\left(\frac{v}{2v_o}\right)}d\phi_\tau(-\tau^2\sin^2\phi_\tau)-\int_0^{v/2}d\tau_x\int_0^{\tau_x\frac{2v_o}{v}\sqrt{1-\left(\frac{v}{2v_o}\right)^2}}d\tau_y(-\tau_y^2)\right]\Pi\left(\frac{v}{2v_o}\right). \tag{99}$$

For the first inner integral we make use of

$$\int_0^{\cos^{-1}z}d\phi\,\sin^2\phi=-\frac{1}{2}z\sqrt{1-z^2}+\frac{1}{2}\cos^{-1}(z). \tag{100}$$

This results in

$$=\frac{-8}{\pi v_o^4}\left[\int_0^{v_o}d\tau\,\frac{-\tau^3}{2}\left(\frac{-v}{2v_o}\sqrt{1-\left(\frac{v}{2v_o}\right)^2}+\cos^{-1}\left(\frac{v}{2a}\right)\right)-\int_0^{v/2}d\tau_x\,\frac{-\tau_x^3}{3}\left(\frac{2v_o}{v}\sqrt{1-\left(\frac{v}{2v_o}\right)^2}\right)^3\right]\Pi\left(\frac{v}{2v_o}\right), \tag{101}$$

$$=\frac{-8}{\pi v_o^4}\left[\frac{-v_o^4}{8}\left(\frac{-v}{2v_o}\sqrt{1-\left(\frac{v}{2v_o}\right)^2}+\cos^{-1}\left(\frac{v}{2v_o}\right)\right)+\frac{v_o^4}{12}\frac{v}{2v_o}\sqrt[3]{1-\left(\frac{v}{2v_o}\right)^2}\right]\Pi\left(\frac{v}{2v_o}\right), \tag{102}$$

$$=\frac{1}{\pi}\left[\cos^{-1}\left(\frac{v}{2v_o}\right)-\frac{1}{3}\left[5-2\left(\frac{v}{2v_o}\right)^2\right]\frac{v}{2v_o}\sqrt{1-\left(\frac{v}{2v_o}\right)^2}\right]\Pi\left(\frac{v}{2v_o}\right). \tag{103}$$

Taking the sum of Eqs. 97 and 103 gives the final result

$$A_2(v)=\frac{2}{\pi}\left\{\cos^{-1}\left(\frac{v}{2v_o}\right)-\left[3-2\left(\frac{v}{2v_o}\right)^2\right]\frac{v}{2v_o}\sqrt{1-\left(\frac{v}{2v_o}\right)^2}\right\}\Pi\left(\frac{v}{2v_o}\right). \tag{104}$$